Accepted Manuscript

Targeted nanoparticle binding & detection in petroleum hydrocarbon impacted porous media

Stuart Linley, Andrew Holmes, Timothy Leshuk, Wanis Nafo, Neil R. Thomson, Adil Al-Mayah, Kevin McVey, Kanwartej Sra, Frank X. Gu

Please cite this article as: Linley, S., Holmes, A., Leshuk, T., Nafo, W., Thomson, N.R., Al-Mayah, A., McVey, K., Sra, K., Gu, F.X., Targeted nanoparticle binding & detection in petroleum hydrocarbon impacted porous media, *Chemosphere* (2018), doi: https://doi.org/10.1016/j.chemosphere.2018.10.046.

This is a PDF file of an unedited manuscript that has been accepted for publication. As a service to our customers we are providing this early version of the manuscript. The manuscript will undergo copyediting, typesetting, and review of the resulting proof before it is published in its final form. Please note that during the production process errors may be discovered which could affect the content, and all legal disclaimers that apply to the journal pertain.

Targeted Nanoparticle Binding & Detection in Petroleum Hydrocarbon Impacted Porous Media

Stuart Linley[a,b], Andrew Holmes[a,b], Timothy Leshuk[a,b], Wanis Nafo[c], Neil R. Thomson[c,]*, Adil Al-Mayah[c], Kevin McVey[d], Kanwartej Sra[d], Frank X. Gu[a,b,]*

[a]Department of Chemical Engineering, [b]Waterloo Institute for Nanotechnology, [c]Department of Civil and Environmental Engineering, University of Waterloo, Waterloo, Ontario, Canada, [d]Chevron Energy Technology Company, Houston, Texas, USA

*Corresponding Author

Abstract

Targeted nanoparticle binding has become a core feature of experimental pharmaceutical product design which enables more efficient payload delivery and enhances medical imaging by accumulating nanoparticles in specific tissues. Environmental remediation and geophysical monitoring encounter similar challenges which may be addressed in part by the adoption of targeted nanoparticle binding strategies. This study illustrates that engineered nanoparticles can bind to crude oil-impacted silica sand, a selective adsorption driven by active targeting based on an amphiphilic polymer coating. This coating strategy resulted in 2 mg/kg attachment to clean silica sand compared to 8 mg/kg attachment to oil-impacted silica sand. It was also shown that modifying the surface coating influenced the binding behaviour of the engineered nanoparticles – more hydrophobic polymers resulted in increased binding. Successful targeting of Pluronic-coated iron oxide nanoparticles to a crude oil and silica sand mixture was demonstrated through a combined quantitative Orbital Emission Spectroscopy mass analysis supported by Vibrating Scanning Magnetometer magnetometry, and a qualitative X-ray micro-computed tomography (CT) visualization approach. These non-destructive characterization techniques facilitated efficient analysis of nanoparticles in porous medium samples with minimal sample preparation, and in the case of X-Ray CT, illustrated how targeted nanoparticle binding may be used to produce 3-D images of contaminated porous media. This work demonstrated successful implementation of nanoparticle

26 targeted binding toward viscous LNAPL such as crude oil in the presence of a porous medium, a step

27 which opens the door to successful application of targeted delivery technology in environmental

28 remediation and monitoring.

Introduction

Targeted binding is a familiar concept in the field of healthcare which typically refers to specific analytes

preferentially binding to specific receptors on cells and tissues(Davis et al., 2008). This observation has

driven innovation in nanomedicine over the past two decades and resulted in functionalized

nanoparticles specifically modified to target diseased tissues and release therapeutic payloads(Petros

and DeSimone, 2010; Srinivasarao et al., 2015). Implementation of a targeted nanoparticle binding

platform provides direct enhancement to therapeutic efficiency and reduces side effects by minimizing

drug action on healthy tissue. Targeted binding can also drive accumulation of nanoparticles in tissue

with specific physical or chemical characteristics which can then be detected using medical imaging

technologies and provide an image of target areas(Gupta and Gupta, 2005; Qin et al., 2007; Rosen et al.,

2012). Soil contamination and its remediation bears many similar challenges to diseased tissue and its

treatment; the impacted site is often not easily accessible, *in situ* treatment wishes to avoid delivering a

payload to clean soil, and the contaminated region has different chemical and physical characteristics

from the surrounding material. By taking advantage of the unique physical and chemical properties of

the impacted region, nanoparticles can be designed to preferentially accumulate there, allowing for

targeted treatment or enhanced imaging.

Soil remediation using materials designed for targeted removal of specific contaminants has been a

subject well studied in the area of toxic metals removal wherein the mobile contaminant species is

adsorbed to a high-surface area nanostructure such as titanate nanotubes or modified graphene

oxide(Chang et al., 2017a; Hu et al., 2017a, 2017c; Linghu et al., 2017). Some graphene oxide-based

strategies introduce the possibility of target contaminant immobilization by forming graphene oxide-

metal ion complexes with enhanced adsorption to mineral material(Chang et al., 2017b; Hu et al.,

2017b; Sheng et al., 2018). Treatment strategies pursuing elimination of fixed contaminants, such as in

the case of viscous non-aqueous phase liquids (NAPLs), require the treatment agent to be emplaced in

3

53   the contaminated region rather than adsorb the contaminant to its surface, and a knowledge gap exists

54   in this regard. Soil contamination by NAPL petroleum hydrocarbons (PHCs) often requires some type of

55   remedial activity to address potential impacts on ecosystems or human health. While conventional *in*

56   *situ* remediation technologies utilizing direct delivery of reagents have been successful in treating some

57   types of PHCs(Jawitz et al., 1998; Salanitro et al., 2000; Sra et al., 2013), options are limited for viscous

58   hydrocarbons such as heavy crude oils, for which no effective *in situ* treatment strategy exists.

59   Advancements in nanotechnology have led to the emergence of nanoremediation which utilizes the

60   higher specific surface area of nanoparticles to achieve faster treatment, but applications are still limited

61   by other drawbacks such as particle self-aggregation and aggregation with mineral material(Karn et al.,

62   2009; Kuppusamy et al., 2016). Nanoremediation treatment of a contaminant may occur directly as a

63   result of nanoparticle contact, as in the case of nZVI(Pardo et al., 2015), or indirectly through Fenton-like

64   catalysis of a persulfate reaction where the nanoparticle supplies leached iron ions(Al-Shamsi and

65   Thomson, 2013). The challenge of delivering nanoparticles to a treatment zone has spurred significant

66   investigation of coating materials to improve their transport properties(Braun et al., 2015; Johnson et

67   al., 2013; Li et al., 2015; Luna et al., 2015; Su et al., 2015); however, these improvements do not

68   guarantee nanoparticle delivery directly to the NAPL interface, and have led to serious discussion

69   regarding the toxicity risks of releasing mobile nanoparticles into an unrestricted environment(Höss et

70   al., 2015; Karn et al., 2009; Tosco et al., 2014). Based on similarities to nanomedicine, *in situ*

71   nanoremediation may be improved by the adoption of targeted binding. To this end, a successful

72   targeted nanoparticle delivery system must be capable of: (1) using nanoparticles that can be tuned to

73   stick or bind to target NAPL mass that they contact, (2) transporting functional nanoparticles in various

74   geologic media over significant distances (i.e., > 1 m), and (3) allowing the bound nanoparticles to be

75   triggered either actively or passively to enable treatment.

76 In general, targeted delivery is divided into two broad categories: passive and active which rely on

77 physical and chemical surface properties of the target zone, respectively(Bertrand et al., 2014; Elkhodiry

78 et al., 2016; Ganta et al., 2008). The targeting mechanism for NAPL PHCs presented in this paper is

79 similar to active targeting seen in drug delivery and achieved by tailoring the nanoparticle surface to

80 interact with the NAPL PHC interface(Saleh et al., 2006). Such an 'active targeting' technique has been

81 previously demonstrated for chlorinated hydrocarbon NAPLs using a block co-polymer nanoparticle

82 surface coating capable of stabilizing nanoparticles in aqueous suspension and promoting hydrophobic

83 interactions(Saleh et al., 2006, 2005; Wang and Acosta, 2013). Targeted delivery of nanoparticles has

84 the potential to further increase the impact and efficiency of nanoremediation techniques by

85 concentrating the reagent in direct contact with the NAPL.

86 In this paper, we report on the selective binding of functional nanoparticles to one class of NAPL PHCs.

87 Specifically, we focussed on the ability of an inexpensive, non-toxic(Singh-Joy and McLain, 2016),

88 amphiphilic block co-polymer coating (Pluronic) applied to iron oxide nanoparticles to promote aqueous

89 stability and hydrophobic interactions with viscous hydrocarbons. Iron oxide nanoparticles were

90 selected as the core material due to their simple synthesis, possible application as an iron catalyst for

91 various chemical oxidation processes (Usman et al., 2012), and capability to act as an energy absorber

92 for thermal treatment strategies (Chien, 2012; Kharisov et al., 2012; Maehara et al., 2005; Zhou et al.,

93 2016). Nanoparticle targeted binding behaviour was assessed using a batch experimental design and

94 quantified indirectly using aqueous-phase concentration measurements. This indirect approach was

95 supported by direct quantification of bound nanoparticles using VSM magnetometry, and binding was

96 further visualized using a qualitative X-ray Computed Tomography (CT) technique.

97 Nanotechnology-enabled sensing techniques are a subject of significant research for detecting

98 contaminants. Through interaction of the nanoparticle with an analyte of interest, a detectable signal

99 can be generated to confirm or measure the presence of the analyte(Zeng et al., 2016; Zhu et al., 2014).

5

100 Using nanoparticles adsorbed to target contaminants in porous media as a contrast agent is a nano-

101 enabled sensing technique analogous to X-Ray CT medical imaging. In the context of geosciences, X-Ray

102 CT relies on identifying areas of varying radiological density which can vary with mineral type(Cnudde et

103 al., 2006), for example, Fe_3O_4 absorbs X-Rays more strongly than SiO_2. The possibility and threshold of

104 detection for nanoparticles in porous media is a key question that must be addressed in the context of

105 X-Ray CT detection of nanoparticles in geologic media. Typical characterization of nanoparticles or trace

106 metals embedded in soil relies on tedious, destructive techniques such as acid digestion and subsequent

107 ICP-MS or ICP-OES analysis(Liu et al., 2017, 2018), prompting research into new analysis techniques

108 which avoid lengthy sample preparation(Kaveh and Beauchemin, 2014; Russo et al., 2002; Senesi et al.,

109 2009). 3-D mapping of nanoparticle accumulation would require performing this type of lengthy analysis

110 multiple times in order to construct a model. With the X-Ray CT technique introduced here, non-

111 destructive 3-D analysis of relatively large samples is achieved with a single, quick, high-resolution scan

112 and minimal sample preparation. This research effort investigates one of the critical features of a

113 potential targeted nanoparticle delivery system, i.e., ability to bind to a target NAPL mass, and

114 demonstrates what a possible end-use of nanoparticle targeted binding might look like through the

115 application of X-Ray CT to detect contaminated sands containing bound nanoparticles. Research that

116 addresses the other two features of a robust targeted delivery platform (transport in various porous

117 media, and activation options for treatment) is ongoing.

118

119 **Materials and Methods**

120 Materials

121 Iron (II) sulfate heptahydrate ($FeSO_4 \cdot 7H_2O$, > 99%), iron (III) chloride hexahydrate ($FeCl_3 \cdot 6H_2O$, > 99%),

122 ammonium hydroxide (NH_4OH, 28-30% in water), dichloromethane (DCM, > 99%), and oleic acid (> 90%)

123 were purchased from Sigma Aldrich (St. Louis, MO, USA). Hydrochloric acid (37%) and ethanol (ACS

124 grade, 99%) were purchased from Fisher Scientific (Hampton, NH, USA). Pluronic co-polymers P104, L62,

125 and L121 (Table 1) were gifted by Brenntag (Essen, Germany) and BASF (Ludwigshafen, Germany). Silica

126 sand (99.7% SiO_2, d_{50} = 0.2 mm) was purchased from Opta Minerals, Inc. (Hamilton, ON, Canada). Crude

127 oil (heavy, sour crude, API gravity 13.3 (ρ = 0.977 g/cm^3), kinematic viscosity 4.745 x 10^{-4} m^2/s @ 40 ^{o}C)

128 was provided by Chevron Energy Technology Company (Houston, TX, USA). All materials were used as

129 received.

Nanoparticle Synthesis

131 Nanoparticle synthesis was adapted from several methods previously reported(Chan and Gu, 2013; Cui

132 et al., 2007; Xu et al., 2006). $FeSO_4 \cdot 7H_2O$ and $FeCl_3 \cdot 6H_2O$ were added to deoxygenated water at a molar

133 ratio of 2:3 ($FeSO_4$:$FeCl_3$). Sufficient NH_4OH and oleic acid were added to achieve final concentrations of

134 4 and 0.22 mol/L, respectively. This solution was stirred at 70 °C for 1 h, then stirred at 90 °C under

135 flowing N_2 for 1 h to purge evolved NH_3 gas. After cooling to room temperature, the black, magnetic

136 precipitate was recovered by magnetic decantation and washed 3x by deoxygenated Millipore DI water

137 (Millipore Elix 5), and then 3x by ethanol before being dried under flowing N_2.

Nanoparticle Phase Transfer

139 A mixture of oleic acid in hexane (1% v/v) was prepared to which dried nanoparticles were added at a

140 concentration of 90 g/L and sonicated for 10 min (VWR "Symphony" 1.9 L Ultrasonic Cleaner). The

141 resulting suspension was added to various aqueous solutions of Pluronic co-polymer(s) at a

142 concentration of 10 % v/v and probe sonicated for 30 min to emulsify the water and hexane phases

143 (Fisher Scientific FB505 Sonic Dismembrator, 200 W). The emulsified nanoparticle sample was

144 transferred to a separatory funnel and separated over 48 h. The resulting aqueous nanoparticle

145 suspension (~3 g/L) was stored until used.

Nanoparticle Binding Studies

147 Oil-impacted silica sand (OSS) was prepared by dissolving crude oil in DCM at a concentration of 60 g/L,

148 mixing it with dry silica sand, and evaporating the DCM such that the final concentration of crude oil in

7

149 sand was 1.5% (m/m). 15 g of OSS was then added to a 20-mL cylindrical glass vial, followed by 10 mL of

150 nanoparticle suspension diluted with Millipore DI water to either 1:100 or 1:10 of its concentration after

151 phase-transfer. The glass vials were then loaded onto an orbital shaker (Stovall Life Sciences "Belly

152 Dancer") for 48 h. Following mixing, the nanoparticle solution was recovered by filtration (1.5 μm glass

153 fiber, Whatman). The retentate was washed with 100 mL Millipore DI water and dried by vacuum

154 desiccation for 96 h before CT, scanning electron microscopy (SEM)/energy dispersive X-ray

155 spectroscopy (EDS), or Vibrating Scanning Magnetometer/ Superconducting Quantum Interference

156 Device (VSM/SQUID) analysis. For control, a "clean" silica sand (SS) sample was prepared identically as

157 above except the DCM/crude oil mixture was not added. Three replicates of each sample were

158 prepared to capture variability. The composition of the different nanoparticle formulations investigated

159 are listed in Table 1. All batch experiments were performed in triplicate.

160 Analyses
161 Aqueous nanoparticle samples were acid digested in 6 mol/L HCl and then diluted by a factor of 10 with

162 1 mol/L HCl prior to analysis by ICP-OES (Prodigy) to quantify total iron (method detection limit (MDL) of

163 4 μg/L). Nanoparticle mass bound on the OSS or the SS (μg of NP/dry g of sand) was estimated from the

164 difference between the initial and final (after 48 h of exposure) nanoparticle concentration.

165 High Resolution Transmission Electron Microscopy (HR-TEM) analysis was performed using a JEOL 2010F

166 with an acceleration voltage of 200 keV. The nanoparticles were dispersed in ethanol, sonicated, and a

167 droplet placed on a holey carbon coated Cu grid, which was allowed to air dry before being analysed.

168 Dynamic Light Scattering (DLS) was used to characterize nanoparticle hydrodynamic size and uniformity.

169 A subsample (3 mL) of the nanoparticle suspension in hexane (prior to Pluronic coating) or in water

170 (after Pluronic coating) was placed into a polypropylene cuvette and analyzed by DLS (Brookhaven

171 90Plus Particle Size Analyzer).

172 Sample magnetization was measured using a Vibrating Scanning Magnetometer (VSM; Quantum Design

173 MPMS 3). Sand samples (as described above) were packed into polycarbonate VSM sample holders.

174 VSM was performed at a temperature of 70 K cooled by liquid N_2 to prevent material movement within

175 the samples and was performed with a maximum magnetic field strength of 1 T. Magnetic properties of

176 nanoparticles required for quantitative analysis were determined using freeze-dried Formulation A

177 particles prepared using a Labconco Freezone 2.5 freeze drier.

178 X-Ray CT samples (as described above) were packed into 4.5-mL polypropylene cuvettes and scanned

179 with an open directional high-power micro-focus X-ray tube (240 kV, GE Phoenix v|tome|x m compact

180 micro CT system) equipped with a GE DXR detector array. X-ray scan parameters (Table S1) were chosen

181 to ensure optimal X-ray penetration and contrast. An acceleration voltage of 80 kV with a beam current

182 of 80 µA resulted in strong visual contrast between iron oxide and silica materials. Raw images were

183 processed using Volume Graphics software (VGStudio Max) as two separate materials (iron oxide and

184 silica) using beam hardening factors between 9.5 and 9.6. Both OSS and SS sample images were

185 processed identically.

186 **Results and Discussion**

187 **Nanoparticle Design**

188 Engineered nanoparticles were designed to facilitate stability in aqueous suspension and favourable

189 interactions with a hydrophobic phase such that particles would bind to the oil-water interface while

190 avoiding adsorption directly to mineral soil material. To achieve this behaviour, an amphiphilic polymer

191 coating was applied to a hydrophobic nanoparticle core (Scheme 1). The nanoparticle core was

192 composed of iron oxide produced via a co-precipitation of iron salts, and made hydrophobic by oleic

193 acid chemisorbed to the iron oxide surface through monodentate chelation of its carboxylate group with

194 iron surface atoms(Wilson and Langell, 2014). This oleic acid layer allows further functionalization by the

195 amphiphilic polymer which is bound to the nanoparticle by hydrophobic forces. The final particle

196 structure allowed favourable thermodynamic interactions between hydrophobic segments of the

197 amphiphilic polymer coating and a NAPL phase, causing nanoparticles to partition to the water/NAPL

198 interface(Saleh et al., 2006, 2005; Wang and Acosta, 2013). Pluronic, an inexpensive, commercially

199 available polymer with highly tunable hydrophobic/hydrophilic properties, was selected as the coating

200 material. Pluronic is a block co-polymer composed of a middle, hydrophobic segment of poly-propylene

201 oxide (PPO) and two outer, hydrophilic segments of poly-ethylene oxide (PEO). The Pluronic coating was

202 attached to the iron oxide core through hydrophobic interactions between the oleic acid nanoparticle

203 capping agent and PPO segments. The PEO segments of the coating extend into the aqueous phase

204 surrounding the nanoparticle and prevent nanoparticle aggregation through steric stabilization. Details

205 regarding the properties of different Pluronic polymers used are given in Table 2. It should be noted that

206 a similar nanoparticle structure using Pluronic F127 has been previously reported in the literature for

207 application in promoting cellular uptake(Lin et al., 2009), however findings in this paper indicate that

208 F127 may not be the most appropriate polymer to promote targeted binding to viscous hydrocarbons,

209 necessitating careful selection of amphiphilic surface coating molecules based on the desired

210 application. L62 and L121 were investigated as more hydrophobic polymers having approximate relative

211 hydrophobic/hydrophilic mass ratios ($M_{n(PPO)}/M_{n(PEO)}$) of 4 and 9, respectively. P104 was investigated as a

212 more hydrophilic polymer having an approximate relative hydrophobic/hydrophilic mass ratio of 1.5.

Nanoparticle Characterization

214 HR-TEM data showed that the nanoparticle iron oxide cores were spherical with an average diameter of

215 6.4 ± 1.8 nm (Figure 1 A), consistent with DLS measurement of particle cores in hexane – 8.4 nm

216 diameter with a polydispersity index (PDI) of 0.260 (Figure S1). After Pluronic coating, the nanoparticle

217 average diameter increased significantly to 120.9 ± 47 nm (Figure 1 B), again supported by a DLS

218 hydrodynamic diameter of 89.8 nm with a PDI of 0.138. This increase in size is attributed to the

219 formation of a miniemulsion of multiple iron oxide cores within a surfactant polymer coating(Cui et al.,

220 2007; Landfester, 2000; Xu et al., 2006). These aggregates form due to the requirement for sufficient

221 surface coverage with surfactant to realize a critically-stable state; smaller particles require higher

222 surfactant concentrations(Landfester, 2000). Although aggregation increased with polymer coating, the

223 dispersity of the particles remained narrow (Figure S1), indicating that aggregation was limited and large

224 aggregates (> 1 μm) were not present. HR-TEM images (Figure 1 C, D) demonstrated the crystallinity of

225 the iron oxide particles individually and within an aggregate structure as indicated by the ordered rows

226 of atoms. In contrast to the order seen within the iron oxide particles, the disordered fringe adjacent to

227 the crystalline region of the nanoparticle observed in Figure 1D is interpreted as an amorphous polymer

228 coating. The thickness of this coating was measured to be 1.1 ± 0.17 nm which compares similarly to the

229 thickness of Pluronic species adsorbed on hydrophobic surfaces through hydrophobic interactions

230 (Brandani and Stroeve, 2003).

Nanoparticle Binding

232 The iron concentration in the filtered solution for nanoparticle Formulation A after exposure to OSS was

233 significantly lower than the same formulation exposed to SS (Figure 2). Compared to the iron

234 concentration of the initial solution (26.2 ± 0.8 mg/L), a reduction of 2.9 ± 1.7 mg/L (11.2%) was

235 observed in the SS solution, and a reduction of 14.8 ± 0.84 mg/L (56.4%) was observed in the OSS

236 solution, indicating preferential nanoparticle adsorption to sand containing NAPL PHC. The estimated

237 mass of nanoparticles bound to the sand after exposure was 1.95 ± 1.15 μg/g on SS, and 7.89 ± 0.56

238 μg/g on OSS. Nanoparticle binding using Formulation A nanoparticles also exceeded binding observed

239 under identical conditions using oleic acid-stabilized particles in the absence of Pluronic (Figure S2)

240 indicating that Pluronic coating was important to the adsorption mechanism. When the particles are

241 stabilized using only oleic acid, a double layer of oleic acid forms around the particles, creating a

242 hydrophilic anionic carboxylate shell preventing interaction with the NAPL PHC. Wang et al. have

11

243 previously shown that addition of a cationic surfactant to an oleate nanoparticle coating system can

244 significantly improve targeted binding to trichloroethylene by disrupting the charge of the bilayer(Wang

245 and Acosta, 2013). A similar likely occurred in this system whereby Pluronic disrupts the oleate bilayer,

246 allowing hydrophobic interaction between the oleate surface and the hydrocarbon/water interface.

247 Furthermore, literature demonstrates that nanoparticle core properties influence particle adsorption

248 behaviour by affecting coating conformation(Hotze et al., 2014). By layering Pluronic on top of oleic acid,

249 we may lessen the effect of the core material on Pluronic conformation, leading to higher applicability of

250 this coating strategy to various nanoparticle core materials. At this point, the mechanism of nanoparticle

251 binding is not fully understood, but is hypothesized to be due to hydrophobic forces from the Pluronic

252 coating, oleate coating, or a combination of both. Any nanoparticle binding to clean sand was attributed

253 to van der Waals forces between the PEO segment of the Pluronic coating and the surface of the SiO_2

254 sand grains. Previous literature suggests hydrogen bonding occurs between the ether oxygen of PEO

255 and the hydroxyl species on the surface of an acidic metal oxide such as SiO_2(Addai-Mensah, 2007). This

256 interaction necessitates that the PEO segments of the Pluronic coating should be short to maintain a

257 strong binding contrast between clean and oil-impacted sands.

258 Direct, quantitative magnetic analysis of dried OSS before and after exposure to Formulation A

259 nanoparticle solution was assessed using VSM. The saturation magnetization of solid Formulation A

260 nanoparticles (required to calculate nanoparticle mass deposition in the sand sample) was measured

261 using freeze-dried nanoparticles (Figure S3) and found to be 59.76 emu/g. The magnetic hysteresis

262 curves for the magnetization of OSS samples as an applied magnetic field is cycled between polarities

263 are shown in Figure 3. The saturation magnetization represents the maximum, steady-state

264 magnetization reached by a sample under a strong magnetic field. The difference between the

265 saturation magnetization in the OSS Control sample and the OSS+NP sample was attributed to the

266 presence of magnetic nanoparticles. This difference was divided by the saturation magnetization of

267 Formulation A nanoparticles to give a mass concentration estimate (g/g) for bound nanoparticles of 8.13

268 ± 0.27 µg/g. This VSM estimate compares closely to the estimate of 7.89 ± 0.56 µg/g determined

269 indirectly by the decrease in iron concentration in the aqueous phase.

270 As the Pluronic hydrophobic/hydrophilic ratio of the nanoparticle coating increased (Table 1), the

271 nanoparticle concentration in aqueous suspension decreased when exposed to OSS, implying greater

272 nanoparticle binding (Figure 4). When compared to Figure 2, the smaller %NP decrease observed for

273 samples in Figure 4 is primarily due to higher initial concentrations used in this binding experiment

274 (estimated NP binding, however, is increased). The results in Figure 4 indicate that nanoparticle binding

275 towards viscous hydrocarbons, specifically heavy crude oil, could be tuned by changing the surface

276 coating formulation. These results are consistent with the behaviour of Pluronic-coated magnetite

277 nanoparticles employed in biomedical applications - previous work using such particles as an MRI

278 contrast agent for tumor imaging reported that Pluronic coating formulation could be adjusted to avoid

279 adsorption to proteins and that a balance between the hydrophobic and hydrophilic characteristics of

280 the polymer is critical to maintaining stability and dispersion(Jain et al., 2009). The trend observed in

281 Figure 4 relating coating hydrophobicity to nanoparticle binding supports the theory that binding is due

282 to hydrophobic interactions as proposed by Saleh et al.(Saleh et al., 2005). While the modification of

283 the particles in this work is different, the interactions which lead to NAPL targeting behaviour remain

284 the same. The larger, longer hydrophobic portions of the surface coating remain contracted in water

285 and swell in the presence of oil, resulting in a more energetically favourable configuration of the particle

286 at the oil/water interface and facilitate targeted binding behaviour.

X-Ray CT Visualization of Nanoparticle Binding

288 SEM characterization of sand following nanoparticle exposure was initially investigated as a direct

289 method to support nanoparticle binding, but it was found that SEM provided insufficient magnification

290 and resolution to observe nanoparticles on the sand surface (Figure S4). SEM/EDS (Energy Dispersive X-

291 ray Spectroscopy) was also investigated for the same purpose (Figure S5), but large sampling areas,

292 restricted magnification and resolution, and overwhelming elemental presence of carbon and silicon

293 restricted use of this technique, prompting investigation into alternative characterization methods.

294 X-ray micro CT was used as a qualitative tool to visualize the presence of nanoparticles bound to dried

295 OSS and SS (as described previously). A set of 2D projection images was acquired during a full rotation of

296 the sample, which was then used to reconstruct a 3D image consisting of volumetric pixels (voxels) using

297 a filtering back-projection algorithm(Feldkamp et al., 1984). Micro-focus tubes defocus the electron

298 beam proportionally to the electric power to prevent the sample from thermal destruction(Gusenbauer

299 et al., 2016). The voxel size estimated by the GE Phoenix X-ray CT machine was determined to be 27.3

300 μm^3 for all scanned samples.

301 The detection of a single iron oxide nanoparticle or nanoparticle aggregate within a voxel resolution >1

302 μm^3 is challenging. This detection method relied on the overall X-ray absorbance of many iron oxide

303 nanoparticles within one voxel to differentiate a response from the absorbance of silica sand, and hence

304 there was a concentration threshold of nanoparticles for which a positive detection can be determined

305 within a single voxel. Based on preliminary studies it was determined that the detection capabilities of

306 the micro CT system with the X-ray scan parameters used could be as low as 1 mg/kg nanoparticles in

307 silica sand (Figures S6 to S8).

308 Formulation A nanoparticle suspension was selected for CT investigation based on the observation that

309 binding improved with coating hydrophobicity (see Figure 4). The bottom-half of the cuvette shown in

310 Figure 5(A-C) was packed with OSS only, while the remaining top-half of the cuvette was packed with

311 OSS that had been exposed to the Formulation A nanoparticle suspension for 48 hours. For baseline

312 comparison, the bottom-half of the cuvette shown in Figure 5(D-F) was packed with SS only, and the

313 top-half of the cuvette was packed with SS that had been exposed to the Formulation A nanoparticle

314 suspension for 48 hours. The packing of two materials in a single cuvette allowed for direct comparison

315 of each sample to its relevant control.

316 Blue colour has been used in Figure 5 to represent regions of high X-ray absorption (higher nanoparticle

317 density) while green has been used for regions of lower X-ray absorption (lower nanoparticle density)

318 within each cuvette. Due to the concentrations of iron oxide nanoparticles used in the binding studies,

319 the threshold difference (between blue and green) was very narrow. As a result, there are sparse blue

320 regions in the lower section of each cuvette which may occur due to variations in packing density. The

321 images in Figure 5 do not depict absolute values of X-ray absorbance, but rather voxels which fall above

322 (blue) and below (green) a uniform selected threshold to illustrate qualitative evidence of nanoparticle

323 binding. All the images in Figure 5 were obtained using identical X-ray CT operating and image

324 processing parameters so that comparative visual contrasts between Figure 5 (A-C) and (D-F) are

325 possible. The increased X-ray absorbance in the top-half of the cuvette shown in Figure 5 (A-C) suggests

326 substantial nanoparticle binding to the OSS. In contrast, the X-ray absorbance observed in Figure 5 (D-F)

327 is minor for the SS that had been exposed to the nanoparticle suspension compared to Figure 5 (A-C),

328 thus corroborating the indirect binding data (Figure 2).

Conclusions

329

330 Demonstrating nanoparticle targeted binding to NAPL PHCs from an aqueous suspension in a porous

331 medium matrix is one of the critical elements of a targeted nanoparticle delivery system with potentially

332 wide-reaching environmental implications. This work demonstrated that nanoparticle targeted binding

333 to crude oil could be controlled as a function of surface properties determined by an amphiphilic

334 polymer coating. Extension of this concept to the broader environmental monitoring and remediation

335 field implies that targeted binding functionality could be applied to various nanoparticle core materials,

336 potentially enhancing existing nanoremediation techniques and enabling the use of targeted contrast

337 agents for advanced site characterization. Immobilization of engineered nanoparticles at the interface

15

338   between the target contaminant mass and water addresses key drawbacks of current *in situ*

339   nanoremediation strategies, namely improving efficiency and cost,(Saleh et al., 2006, 2005) as well as

340   limiting uncontrolled nanoparticle release(Tosco et al., 2014).

341   The application of X-ray CT to detect nanoparticles in a porous medium has great potential for further

342   development. In this study, there are two notable implications to be drawn from X-ray CT visualization

343   of nanoparticle binding. First, X-ray CT is introduced as a useful, non-destructive technique for quickly

344   analyzing 3-D sand characteristics with minimal sample preparation. Second, it implies a useful

345   application for nanoparticle targeted binding in porous media, that is, as a contrast agent for 3-D

346   imaging of sands impacted with viscous heavy hydrocarbons such as crude oil. Based on these findings,

347   it is conceivable that mobile nanoparticles may be visualized by X-Ray CT in dynamic transport studies.

348   Such experiments may generate a wealth of data to further understanding of nanoparticle transport

349   behaviour in porous media and characterize targeted nanoparticle binding in realistic hydrogeologic

350   conditions. One current drawback of the technique as presented here is its qualitative nature, but with

351   careful development of a proper analysis methodology, it may be possible to extract quantitative data

352   from this technique. In a similar vein, the use of SQUID/VSM magnetic characterization introduces quick,

353   non-destructive, quantitative analysis techniques with minimal sample preparation which may help to

354   overcome difficulties with characterizing nanoparticle presence in sand samples.

355   The work presented here limits its scope to batch investigation and novel X-ray characterization as a

356   proof-of-concept for a targeted binding strategy, but these findings open the door to larger scale

357   experiments under more realistic conditions. The nanoparticle coating proposed here has demonstrated

358   limited binding to clean silica sand implying that transport through porous media should be possible,

359   however literature has demonstrated that interactions with natural macromolecules can change the

360   surface of engineered nanoparticles, affecting their behaviour and fate in soils(Louie et al., 2016). To this

361   end, research investigating the transport properties of these nanoparticles in various porous media, as

362 well as expanded application of this novel X-ray CT nanoparticle characterization technique is ongoing in

363 pursuit of improving and demonstrating the application of this targeted delivery platform for

364 nanoremediation and geophysical monitoring.

Associated Content

365

366 **Supporting Information:**

367 Additional characterization such as DLS to measure particle size in solution, SEM/EDS of clean/oily sand

368 after nanoparticle incubation, and X-ray micro CT of NP-impregnated sand samples to examine

369 thresholds as well as additional information on X-ray CT parameters are available free of charge via the

370 Internet.

Author Information

371

372 **Corresponding Author:**

373 Frank Gu, Department of Chemical Engineering, 200 University Ave. W, Waterloo, ON, Canada, N2L 3G1.
374 Tel: (519) 888-4567 ext. 38605. Fax (519) 888-4347. Email: frank.gu@uwaterloo.ca

375 Neil R. Thomson, Department of Civil & Environmental Engineering, 200 University Ave. W, Waterloo,
376 ON, Canada, N2L 3G1. Tel: (519) 888-4567 ext. 32111. Fax (519) 888-4349. Email:
377 neil.thomson@uwaterloo.ca

378 **Notes:**

379 The authors declare no competing financial interest.

References

Addai-Mensah, J., 2007. Enhanced flocculation and dewatering of clay mineral dispersions. Powder Technol. 179, 73–78. https://doi.org/10.1016/j.powtec.2006.11.008

Al-Shamsi, M.A., Thomson, N.R., 2013. Treatment of Organic Compounds by Activated Persulfate Using Nanoscale Zerovalent Iron. Ind. Eng. Chem. Res. 52, 13564–13571. https://doi.org/10.1021/ie400387p

Bertrand, N., Wu, J., Xu, X., Kamaly, N., Farokhzad, O.C., 2014. Cancer nanotechnology: The impact of passive and active targeting in the era of modern cancer biology. Adv. Drug Deliv. Rev. 66, 2–25. https://doi.org/10.1016/j.addr.2013.11.009

Brandani, P., Stroeve, P., 2003. Adsorption and Desorption of PEO−PPO−PEO Triblock Copolymers on a Self-Assembled Hydrophobic Surface. Macromolecules 36, 9492–9501. https://doi.org/10.1021/ma0342675

Braun, A., Klumpp, E., Azzam, R., Neukum, C., 2015. Transport and deposition of stabilized engineered silver nanoparticles in water saturated loamy sand and silty loam. Sci. Total Environ. 535, 102–112. https://doi.org/10.1016/j.scitotenv.2014.12.023

Chan, T., Gu, F., 2013. Development of a colorimetric, superparamagnetic biosensor for the capture and detection of biomolecules. Biosens. Bioelectron. 42, 12–16. https://doi.org/10.1016/j.bios.2012.10.008

Chang, K., Li, X., Liao, Q., Hu, B., Hu, J., Sheng, G., Linghu, W., Huang, Y., Asiri, A.M., Alamry, K.A., 2017a. Molecular insights into the role of fulvic acid in cobalt sorption onto graphene oxide and reduced graphene oxide. Chem. Eng. J. 327, 320–327. https://doi.org/10.1016/j.cej.2017.06.100

Chang, K., Sun, Y., Ye, F., Li, X., Sheng, G., Zhao, D., Linghu, W., Li, H., Liu, J., 2017b. Macroscopic and molecular study of the sorption and co-sorption of graphene oxide and Eu(III) onto layered double hydroxides. Chem. Eng. J. 325, 665–671. https://doi.org/10.1016/j.cej.2017.05.122

Chien, Y.-C., 2012. Field study of in situ remediation of petroleum hydrocarbon contaminated soil on site using microwave energy. J. Hazard. Mater. 199–200, 457–461. https://doi.org/10.1016/j.jhazmat.2011.11.012

Cnudde, V., Masschaele, B., Dierick, M., Vlassenbroeck, J., Hoorebeke, L.V., Jacobs, P., 2006. Recent progress in X-ray CT as a geosciences tool. Appl. Geochem., Frontiers in Analytical Geochemistry–An IGC 2004 Perspective 21, 826–832. https://doi.org/10.1016/j.apgeochem.2006.02.010

Cui, L., Xu, H., He, P., Sumitomo, K., Yamaguchi, Y., Gu, H., 2007. Developing a hybrid emulsion polymerization system to synthesize Fe3O4/polystyrene latexes with narrow size distribution and high magnetite content. J. Polym. Sci. Part Polym. Chem. 45, 5285–5295. https://doi.org/10.1002/pola.22273

Davis, M.E., Chen, Z. (Georgia), Shin, D.M., 2008. Nanoparticle therapeutics: an emerging treatment modality for cancer. Nat. Rev. Drug Discov. 7, 771–782. https://doi.org/10.1038/nrd2614

Elkhodiry, M.A., Momah, C.C., Suwaidi, S.R., Gadalla, D., Martins, A.M., Vitor, R.F., Husseini, G.A., 2016. Synergistic Nanomedicine: Passive, Active, and Ultrasound-Triggered Drug Delivery in Cancer Treatment. J. Nanosci. Nanotechnol. 16, 1–18. https://doi.org/10.1166/jnn.2016.11124

Feldkamp, L.A., Davis, L.C., Kress, J.W., 1984. Practical cone-beam algorithm. J. Opt. Soc. Am. 1, 612–619. https://doi.org/10.1364/JOSAA.1.000612

Ganta, S., Devalapally, H., Shahiwala, A., Amiji, M., 2008. A review of stimuli-responsive nanocarriers for drug and gene delivery. J. Controlled Release 126, 187–204. https://doi.org/10.1016/j.jconrel.2007.12.017

434 Gupta, A.K., Gupta, M., 2005. Synthesis and surface engineering of iron oxide nanoparticles for
435   biomedical applications. Biomaterials 26, 3995–4021.
436   https://doi.org/10.1016/j.biomaterials.2004.10.012
437 Gusenbauer, C., Reiter, M., Kastner, J., Kloesch, G., 2016. Detection of Non-Metallic Inclusions in
438   Quenched and Tempered Steel Bars by XCT and after Fatigue Life Testing. Steel Res. Int. 87,
439   386–393. https://doi.org/10.1002/srin.201500083
440 Höss, S., Fritzsche, A., Meyer, C., Bosch, J., Meckenstock, R.U., Totsche, K.U., 2015. Size- and
441   Composition-Dependent Toxicity of Synthetic and Soil-Derived Fe Oxide Colloids for the
442   Nematode *Caenorhabditis elegans*. Environ. Sci. Technol. 49, 544–552.
443   https://doi.org/10.1021/es503559n
444 Hotze, E.M., Louie, S.M., Lin, S., Wiesner, M.R., Lowry, G.V., 2014. Nanoparticle core properties affect
445   attachment of macromolecule-coated nanoparticles to silica surfaces. Environ. Chem. 11, 257.
446   https://doi.org/10.1071/EN13191
447 Hu, B., Chen, G., Jin, C., Hu, J., Huang, C., Sheng, J., Sheng, G., Ma, J., Huang, Y., 2017a. Macroscopic and
448   spectroscopic studies of the enhanced scavenging of Cr(VI) and Se(VI) from water by titanate
449   nanotube anchored nanoscale zero-valent iron. J. Hazard. Mater. 336, 214–221.
450   https://doi.org/10.1016/j.jhazmat.2017.04.069
451 Hu, B., Huang, C., Li, X., Sheng, G., Li, H., Ren, X., Ma, J., Wang, J., Huang, Y., 2017b. Macroscopic and
452   spectroscopic insights into the mutual interaction of graphene oxide, Cu(II), and Mg/Al layered
453   double hydroxides. Chem. Eng. J. 313, 527–534. https://doi.org/10.1016/j.cej.2016.12.102
454 Hu, B., Qiu, M., Hu, Q., Sun, Y., Sheng, G., Hu, J., Ma, J., 2017c. Decontamination of Sr(II) on Magnetic
455   Polyaniline/Graphene Oxide Composites: Evidence from Experimental, Spectroscopic, and
456   Modeling Investigation. ACS Sustain. Chem. Eng. 5, 6924–6931.
457   https://doi.org/10.1021/acssuschemeng.7b01126
458 Jain, T.K., Foy, S.P., Erokwu, B., Dimitrijevic, S., Flask, C.A., Labhasetwar, V., 2009. Magnetic resonance
459   imaging of multifunctional pluronic stabilized iron-oxide nanoparticles in tumor-bearing mice.
460   Biomaterials 30, 6748–6756. https://doi.org/10.1016/j.biomaterials.2009.08.042
461 Jawitz, J.W., Annable, M.D., Rao, P.S.C., Rhue, R.D., 1998. Field Implementation of a Winsor Type I
462   Surfactant/Alcohol Mixture for in Situ Solubilization of a Complex LNAPL as a Single-Phase
463   Microemulsion. Environ. Sci. Technol. 32, 523–530. https://doi.org/10.1021/es970507i
464 Johnson, R.L., Nurmi, J.T., O'Brien Johnson, G.S., Fan, D., O'Brien Johnson, R.L., Shi, Z., Salter-Blanc, A.J.,
465   Tratnyek, P.G., Lowry, G.V., 2013. Field-Scale Transport and Transformation of
466   Carboxymethylcellulose-Stabilized Nano Zero-Valent Iron. Environ. Sci. Technol. 47, 1573–1580.
467   https://doi.org/10.1021/es304564q
468 Karn, B., Kuiken, T., Otto, M., 2009. Nanotechnology and in Situ Remediation: A Review of the Benefits
469   and Potential Risks. Environ. Health Perspect. 117, 1823–1831.
470 Kaveh, F., Beauchemin, D., 2014. Improvement of the capabilities of solid sampling ETV-ICP-OES by
471   coupling ETV to a nebulisation/pre-evaporation system. J. Anal. At. Spectrom. 29, 1371–1377.
472   https://doi.org/10.1039/C4JA00041B
473 Kharisov, B.I., Dias, H.V.R., Kharissova, O.V., Jiménez-Pérez, V.M., Pérez, B.O., Flores, B.M., 2012. Iron-
474   containing nanomaterials: synthesis, properties, and environmental applications. RSC Adv. 2,
475   9325–9358. https://doi.org/10.1039/C2RA20812A
476 Kuppusamy, S., Palanisami, T., Megharaj, M., Venkateswarlu, K., Naidu, R., 2016. Ex-Situ Remediation
477   Technologies for Environmental Pollutants: A Critical Perspective, in: de Voogt, P. (Ed.), Reviews
478   of Environmental Contamination and Toxicology Volume 236. Springer International Publishing,
479   Cham, pp. 117–192.

480 Landfester, K., 2000. Recent developments in miniemulsions — formation and stability mechanisms.
481   Macromol. Symp. 150, 171–178. https://doi.org/10.1002/1521-3900(200002)150:1<171::AID-
482   MASY171>3.0.CO;2-D
483 Li, J., Bhattacharjee, S., Ghoshal, S., 2015. The effects of viscosity of carboxymethyl cellulose on
484   aggregation and transport of nanoscale zerovalent iron. Colloids Surf. Physicochem. Eng. Asp.
485   481, 451–459. https://doi.org/10.1016/j.colsurfa.2015.05.023
486 Lin, J.-J., Chen, J.-S., Huang, S.-J., Ko, J.-H., Wang, Y.-M., Chen, T.-L., Wang, L.-F., 2009. Folic acid–Pluronic
487   F127 magnetic nanoparticle clusters for combined targeting, diagnosis, and therapy
488   applications. Biomaterials 30, 5114–5124. https://doi.org/10.1016/j.biomaterials.2009.06.004
489 Linghu, W., Yang, H., Sun, Y., Sheng, G., Huang, Y., 2017. One-Pot Synthesis of LDH/GO Composites as
490   Highly Effective Adsorbents for Decontamination of U(VI). ACS Sustain. Chem. Eng. 5, 5608–
491   5616. https://doi.org/10.1021/acssuschemeng.7b01303
492 Liu, J., Luo, X., Wang, J., Xiao, T., Chen, D., Sheng, G., Yin, M., Lippold, H., Wang, C., Chen, Y., 2017.
493   Thallium contamination in arable soils and vegetables around a steel plant—A newly-found
494   significant source of Tl pollution in South China. Environ. Pollut. 224, 445–453.
495   https://doi.org/10.1016/j.envpol.2017.02.025
496 Liu, J., Luo, X., Wang, J., Xiao, T., Yin, M., Belshaw, N.S., Lippold, H., Kong, L., Xiao, E., Bao, Z., Li, N., Chen,
497   Y., Linghu, W., 2018. Provenance of uranium in a sediment core from a natural reservoir, South
498   China: Application of Pb stable isotope analysis. Chemosphere 193, 1172–1180.
499   https://doi.org/10.1016/j.chemosphere.2017.11.131
500 Louie, S.M., Tilton, R.D., Lowry, G.V., 2016. Critical review: impacts of macromolecular coatings on
501   critical physicochemical processes controlling environmental fate of nanomaterials. Environ. Sci.
502   Nano 3, 283–310. https://doi.org/10.1039/C5EN00104H
503 Luna, M., Gastone, F., Tosco, T., Sethi, R., Velimirovic, M., Gemoets, J., Muyshondt, R., Sapion, H., Klaas,
504   N., Bastiaens, L., 2015. Pressure-controlled injection of guar gum stabilized microscale
505   zerovalent iron for groundwater remediation. J. Contam. Hydrol., Fate and Transport of
506   Biocolloids and Nanoparticles in Soil and Groundwater Systems 181, 46–58.
507   https://doi.org/10.1016/j.jconhyd.2015.04.007
508 Maehara, T., Konishi, K., Kamimori, T., Aono, H., Hirazawa, H., Naohara, T., Nomura, S., Kikkawa, H.,
509   Watanabe, Y., Kawachi, K., 2005. Selection of ferrite powder for thermal coagulation therapy
510   with alternating magnetic field. J. Mater. Sci. 40, 135–138. https://doi.org/10.1007/s10853-005-
511   5698-x
512 Pardo, F., Rosas, J.M., Santos, A., Romero, A., 2015. Remediation of a Biodiesel Blend-Contaminated Soil
513   with Activated Persulfate by Different Sources of Iron. Water. Air. Soil Pollut. 226, 1–12.
514   https://doi.org/10.1007/s11270-014-2267-4
515 Petros, R.A., DeSimone, J.M., 2010. Strategies in the design of nanoparticles for therapeutic applications.
516   Nat. Rev. Drug Discov. 9, 615–627. https://doi.org/10.1038/nrd2591
517 Qin, J., Laurent, S., Jo, Y.S., Roch, A., Mikhaylova, M., Bhujwalla, Z.M., Muller, R.N., Muhammed, M.,
518   2007. A High-Performance Magnetic Resonance ImagingT2 Contrast Agent. Adv. Mater. 19,
519   1874–1878. https://doi.org/10.1002/adma.200602326
520 Rosen, J.E., Chan, L., Shieh, D.-B., Gu, F.X., 2012. Iron oxide nanoparticles for targeted cancer imaging
521   and diagnostics. Nanomedicine Nanotechnol. Biol. Med. 8, 275–290.
522   https://doi.org/10.1016/j.nano.2011.08.017
523 Russo, R.E., Mao, X., Liu, H., Gonzalez, J., Mao, S.S., 2002. Laser ablation in analytical chemistry—a
524   review. Talanta 57, 425–451. https://doi.org/10.1016/S0039-9140(02)00053-X
525 Salanitro, J.P., Johnson, P.C., Spinnler, G.E., Maner, P.M., Wisniewski, H.L., Bruce, C., 2000. Field-Scale
526   Demonstration of Enhanced MTBE Bioremediation through Aquifer Bioaugmentation and
527   Oxygenation. Environ. Sci. Technol. 34, 4152–4162. https://doi.org/10.1021/es000925e

528 Saleh, N., Phenrat, T., Sirk, K., Dufour, B., Ok, J., Sarbu, T., Matyjaszewski, K., Tilton, R.D., Lowry, G.V.,
529   2005. Adsorbed Triblock Copolymers Deliver Reactive Iron Nanoparticles to the Oil/Water
530   Interface. Nano Lett. 5, 2489–2494. https://doi.org/10.1021/nl0518268
531 Saleh, N., Sirk, K., Liu, Y., Phenrat, T., Dufour, B., Matyjaszewski, K., Tilton, R.D., Lowry, G.V., 2006.
532   Surface Modifications Enhance Nanoiron Transport and NAPL Targeting in Saturated Porous
533   Media. Environ. Eng. Sci. 24, 45–57. https://doi.org/10.1089/ees.2007.24.45
534 Senesi, G.S., Dell'Aglio, M., Gaudiuso, R., De Giacomo, A., Zaccone, C., De Pascale, O., Miano, T.M.,
535   Capitelli, M., 2009. Heavy metal concentrations in soils as determined by laser-induced
536   breakdown spectroscopy (LIBS), with special emphasis on chromium. Environ. Res. 109, 413–
537   420. https://doi.org/10.1016/j.envres.2009.02.005
538 Sheng, G., Huang, C., Chen, G., Sheng, J., Ren, X., Hu, B., Ma, J., Wang, X., Huang, Y., Alsaedi, A., Hayat,
539   T., 2018. Adsorption and co-adsorption of graphene oxide and Ni(II) on iron oxides: A
540   spectroscopic and microscopic investigation. Environ. Pollut. 233, 125–131.
541   https://doi.org/10.1016/j.envpol.2017.10.047
542 Singh-Joy, S.D., McLain, V.C., 2016. Safety Assessment of Poloxamers 101, 105, 108, 122, 123, 124, 181,
543   182, 183, 184, 185, 188, 212, 215, 217, 231, 234, 235, 237, 238, 282, 284, 288, 331, 333, 334,
544   335, 338, 401, 402, 403, and 407, Poloxamer 105 Benzoate, and Poloxamer 182 Dibenzoate as
545   Used in Cosmetics. Int. J. Toxicol. https://doi.org/10.1080/10915810802244595
546 Sra, K.S., Thomson, N.R., Barker, J.F., 2013. Persulfate injection into a gasoline source zone. J. Contam.
547   Hydrol. 150, 35–44. https://doi.org/10.1016/j.jconhyd.2013.03.007
548 Srinivasarao, M., Galliford, C.V., Low, P.S., 2015. Principles in the design of ligand-targeted cancer
549   therapeutics and imaging agents. Nat. Rev. Drug Discov. 14, 203–219.
550   https://doi.org/10.1038/nrd4519
551 Su, Y., Zhao, Y.-S., Li, L.-L., Qin, C.-Y., 2015. Enhanced Delivery of Nanoscale Zero-Valent Iron in Porous
552   Media by Sodium Dodecyl Sulfate Solution and Foam. Environ. Eng. Sci. 32, 684–693.
553   https://doi.org/10.1089/ees.2014.0529
554 Tosco, T., Petrangeli Papini, M., Cruz Viggi, C., Sethi, R., 2014. Nanoscale zerovalent iron particles for
555   groundwater remediation: a review. J. Clean. Prod., Emerging industrial processes for water
556   management 77, 10–21. https://doi.org/10.1016/j.jclepro.2013.12.026
557 Usman, M., Faure, P., Hanna, K., Abdelmoula, M., Ruby, C., 2012. Application of magnetite catalyzed
558   chemical oxidation (Fenton-like and persulfate) for the remediation of oil hydrocarbon
559   contamination. Fuel 96, 270–276. https://doi.org/10.1016/j.fuel.2012.01.017
560 Wang, Z., Acosta, E., 2013. Formulation design for target delivery of iron nanoparticles to TCE zones. J.
561   Contam. Hydrol. 155, 9–19. https://doi.org/10.1016/j.jconhyd.2013.08.005
562 Wilson, D., Langell, M.A., 2014. XPS analysis of oleylamine/oleic acid capped Fe3O4 nanoparticles as a
563   function of temperature. Appl. Surf. Sci. 303, 6–13.
564   https://doi.org/10.1016/j.apsusc.2014.02.006
565 Xu, H., Cui, L., Tong, N., Gu, H., 2006. Development of High Magnetization Fe3O4/Polystyrene/Silica
566   Nanospheres via Combined Miniemulsion/Emulsion Polymerization. J. Am. Chem. Soc. 128,
567   15582–15583. https://doi.org/10.1021/ja066165a
568 Zeng, G., Zhu, Y., Zhang, Y., Zhang, C., Tang, L., Guo, P., Zhang, L., Yuan, Y., Cheng, M., Yang, C., 2016.
569   Electrochemical DNA sensing strategy based on strengthening electronic conduction and a signal
570   amplifier carrier of nanoAu/MCN composited nanomaterials for sensitive lead detection.
571   Environ. Sci. Nano 3, 1504–1509. https://doi.org/10.1039/C6EN00323K
572 Zhou, H., Hu, L., Wan, J., Yang, R., Yu, X., Li, H., Chen, J., Wang, L., Lu, X., 2016. Microwave-enhanced
573   catalytic degradation of p-nitrophenol in soil using MgFe2O4. Chem. Eng. J. 284, 54–60.
574   https://doi.org/10.1016/j.cej.2015.08.103

575   Zhu, Y., Zeng, G., Zhang, Y., Tang, L., Chen, J., Cheng, M., Zhang, L., He, L., Guo, Y., He, X., Lai, M., He, Y.,
576   2014. Highly sensitive electrochemical sensor using a MWCNTs/GNPs-modified electrode for
577   lead (II) detection based on Pb2+-induced G-rich DNA conformation. Analyst 139, 5014–5020.
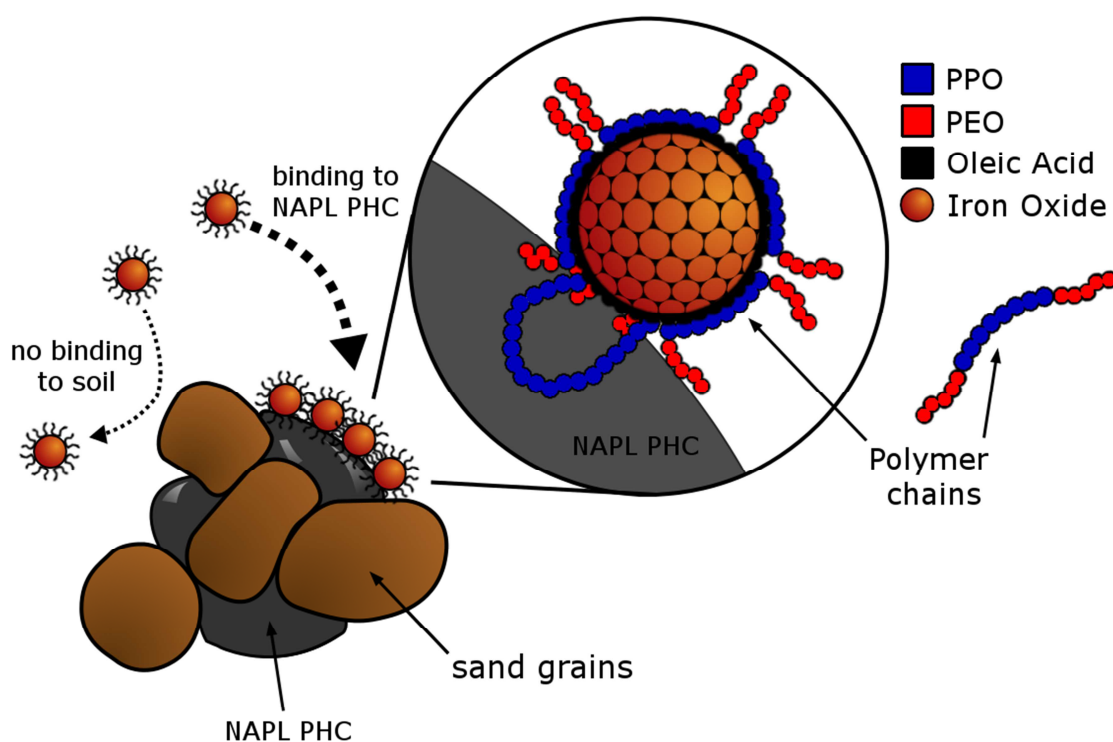578   https://doi.org/10.1039/C4AN00874J
579

580

Figures & Tables
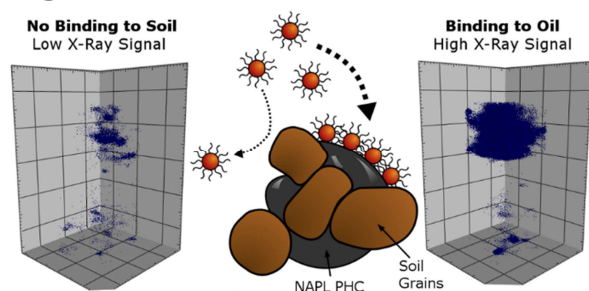
Graphical Abstract. Engineered nanoparticles preferentially attach to NAPL PHC over soil grains. This is observed through higher X-ray CT signal when NP are exposed to oil-impacted sand (right) compared to clean sand (left).

Scheme 1. Schematic illustrating nanoparticles with an amphiphilic polymer coating (Pluronic) avoiding adsorption to sand grains and specifically adsorbing to NAPL PHC through hydrophobic interactions. Polyethylene Oxide (PEO; red) blocks of the coating extend into the aqueous phase and contract in the NAPL PHC. Polypropylene Oxide (PPO; blue) blocks of the coating extend into the NAPL PHC and contract in the aqueous phase. Oleic acid (black) binds the coating to the nanoparticle surface and interacts favourably with the NAPL PHC when at the interface.

Table 1. Summary of nanoparticle formulations explored.

formulation ID[a]	Pluronic L62 (g/L)[b]	Pluronic L121 (g/L)[b]	Pluronic P104 (g/L)[b]	Dynamic Light Scattering diameter (nm)
A (A-100)	10	-	-	89.80
B-40	4	-	6	64.42
B-60	6	-	4	57.60
B-80	8	-	2	61.60
C-40	2	2	6	75.61
C-60	3	3	4	82.68
C-80	4	4	2	81.16

594   [a] Oleic acid is a common component of all formulations, present at a concentration of 0.1% v/v

595   [b] concentration in aqueous solution prior to nanoparticle phase transfer.

596

597   **Table 2.** Properties of Pluronic polymers used for amphiphilic nanoparticle coating

| Polymer ID	M_n (g/mol)	Structure	M_n of PPO (g/mol)	M_n of PEO (g/mol)	$M_{n(PPO)}$/ $M_{n(PEO)}$
L62	2,250	PEO_5-PPO_{31}-PEO_5	1,800	450	4
L121	4,000	PEO_5-PPO_{62}-PEO_5	3,600	400	9
P104	5,000	PEO_{23}-PPO_{52}-PEO_{23}	3,000	2,000	1.5

598
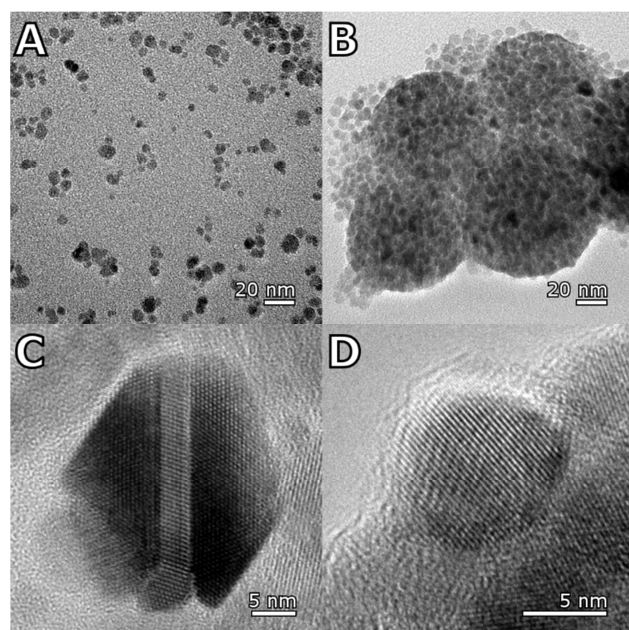
600   **Figure 1.** HR-TEM image of sample A-100: **A** Iron oxide nanoparticles prior to Pluronic coating, **B** Clusters
601   of iron oxide nanoparticles after Pluronic coating, **C** Iron oxide nanoparticle prior to Pluronic coating,
602   and **D** Edge of a Pluronic coated nanoparticle aggregate demonstrating crystalline nanoparticles within
603   an amorphous polymer coating.
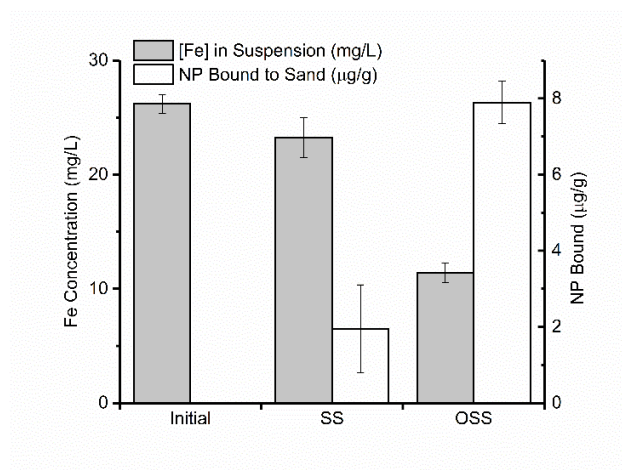
Figure 2. ICP-OES results demonstrating preferential binding of nanoparticle Formulation A to OSS when compared to SS. Iron concentration in suspension was measured directly using ICP-OES. NP bound to sand was calculated indirectly using the observed decrease of iron in the suspension. Error bars represent ± one standard error.
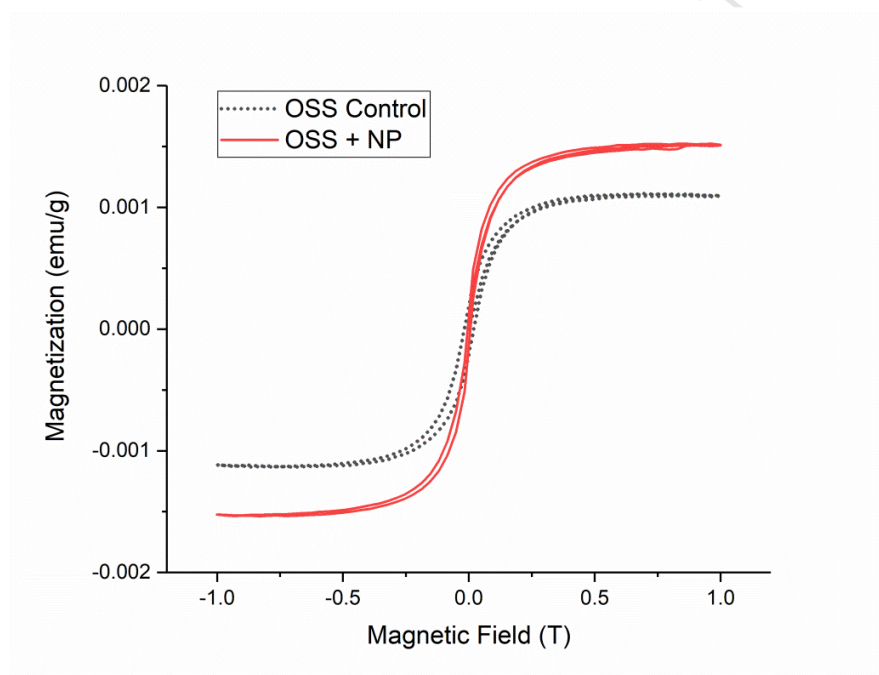

Figure 3. Magnetic hysteresis curves for OSS before (OSS Control) and after exposure to Formulation A nanoparticle solution (OSS + NP). The saturation magnetization was $1.037 \pm 0.016 \times 10^{-3}$ emu/g for the OSS Control sample, and $1.523 \pm 0.016 \times 10^{-3}$ emu/g for the OSS+NP sample.

613
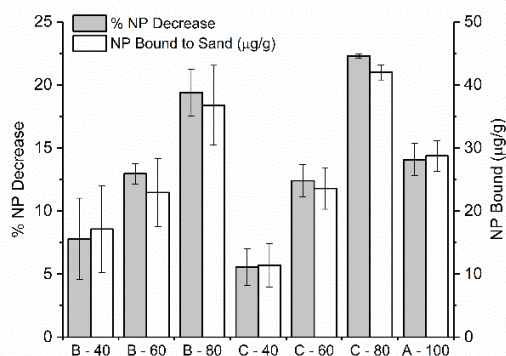
Figure 4. Indirectly calculated nanoparticle (NP) binding increases as nanoparticle coating formulation becomes more hydrophobic. The nomenclature X-# identifies nanoparticle samples (Table 1): X indicates the types of Pluronic in the formulation (A: L62, B: P104+L62, C: P104+L62+L121), and # indicates the percentage of the Pluronics in the formulation with higher relative hydrophobic content (L62 + L121).

618
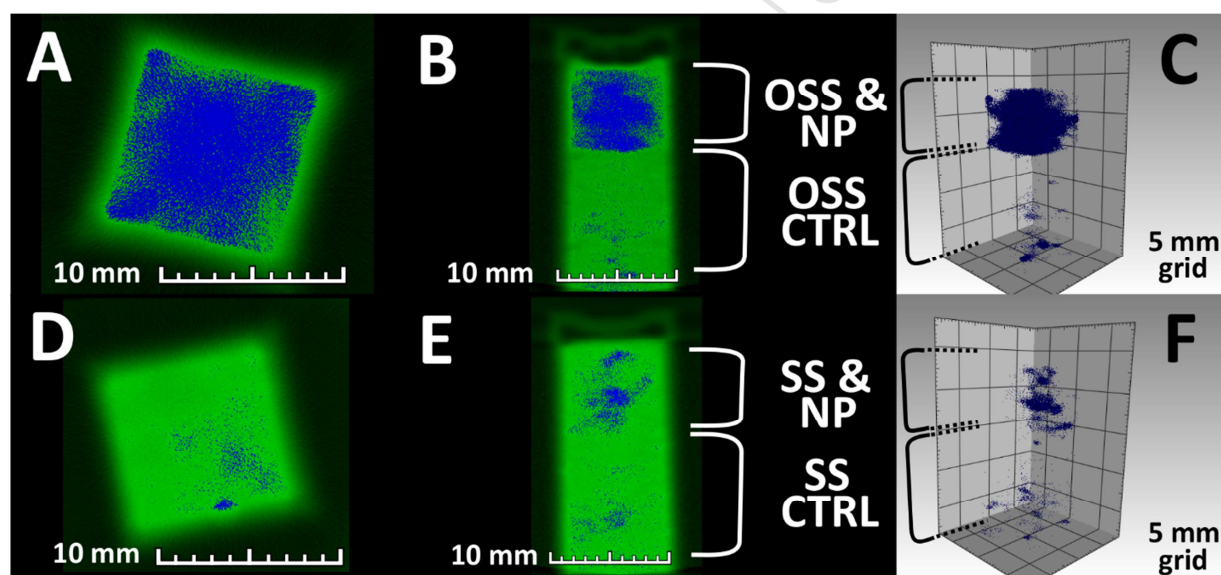
Figure 5. X-ray Computed Tomography of Oil-impacted Silica Sand (OSS; **A**, **B**, and **C**) and Silica Sand (SS; **D**, **E**, and **F**) samples. In each cuvette, the top portion contains sand contacted with Formulation A nanoparticles for 48 h, filtered, washed, and dried while the bottom portion contains the respective control (CTRL) sand, as indicated in **B** and **E**. **A** and **D** show the top view of each cuvette packed with OSS and SS, respectively. **B** and **E** show the side view of each cuvette packed with OSS and SS, respectively. **C** and **F** show a 3-D volumetric reconstruction of each cuvette for OSS and SS, respectively.

625

- Nanoparticles with polymer coating selectively adsorb to impacted sand
- Changing polymer coating composition influences adsorption behaviour
- Nanoparticles detected in impacted sand using novel application of X-Ray CT
- Targeted binding to crude oil in the presence of silica sand at ambient temperature